Briefly, 1 μg of phycoerythrin-labeled tetrameric Mamu-A*01/peptide complexes was used in conjunction with fluorescein isothiocyanate (FITC)–labeled anti-human CD8α (Leu2a; Becton-Dickinson), ECD-labeled anti-human CD8αβ (2ST8-5H7; Beckman Coulter), and APC-labeled anti-rhesus monkey CD3 (FN18; Biosource) monoclonal antibodies to stain peptide-specific $CD8^+$ T cells. Whole blood (100 μl) from the vaccinated monkeys was directly stained with these reagents, then lysed, washed, and fixed. Samples were analyzed by four-color flow cytometry on a Coulter EPICS Elite ESP system, and gated $CD3^+CD8^+$ T cells were examined for staining with tetrameric Mamu-A*01/p11C, Mamu-A*01/p41A, or Mamu-A*01/p68A complexes.

31. D. H. Barouch *et al.*, data not shown.
32. K. A. Reimann *et al.*, *J. Virol.* **70**, 3198 (1996).
33. K. A. Reimann *et al.*, *J. Virol.* **70**, 6922 (1996).
34. K. A. Reimann *et al.*, *Virology* **256**, 15 (1999).
35. J. M. Crawford *et al.*, *J. Virol.* **73**, 10199 (1999).
36. Statistical analysis was performed with GraphPad Prism, version 2.01 (GraphPad Software, Inc., 1996). $CD4^+$ T lymphocyte counts and viral loads were compared between groups by two-sided Wilcoxon rank-sum tests with Bonferroni adjustments of *P* values to account for the two major comparisons of each endpoint. Day 70 setpoint values were chosen in order to analyze a complete data set prior to death of any animals. Differences in clinical events and mortality were analyzed by two-sided Fisher exact tests. Correlations of prechallenge vaccine-elicited CTLs and postchallenge peak CTLs or setpoint viral loads were assessed in the vaccinated monkeys by two-sided Spearman rank correlation tests. In all cases, $P < 0.05$ was considered significant.
37. Intracellular cytokine staining assays were performed as follows. We placed 2×10^6 PBMCs in 17 mm by 100 mm polypropylene tubes containing 1 ml of supplemented RPMI medium, to which 1 μg of each costimulatory antibody (anti-CD28 and anti-CD49d, Becton-Dickinson) was added. Peptide pools were added at a final concentration of 2 μg/ml. Culture tubes were incubated at a 5° slant at 37°C in a humidified 5% CO_2 incubator for 16 hours. Brefeldin A (Sigma) was added for the last 15 hours at a final concentration of 10 μg/ml. Cells were stained with anti–CD3-APC (FN18, Biosource), anti–CD4-PE (OKT4, Ortho Diagnostics), and anti–CD8-PerCP (SK1, Becton-Dickinson) for 30 min and washed with phosphate-buffered saline containing 1% fetal bovine serum. Cells were permeabilized with FACS Permeabilization Buffer (Becton-Dickinson), washed, and stained with anti–IFN-γ–FITC (MD1, Biosource) for 30 min. Samples were fixed in 1% formaldehyde and analyzed on a FACSCalibur flow cytometer (Becton-Dickinson). In order to measure responses of $CD4^+$ T lymphocytes, 30,000 gated $CD3^+CD4^+$ lymphocytes were analyzed for intracellular IFN-γ staining events using CellQuest software (Becton-Dickinson).
38. A. Seth *et al.*, *J. Virol.* **74**, 2502 (2000).
39. M. S. Wyand *et al.*, *J. Virol.* **73**, 8356 (1999).
40. R. A. Koup *et al.*, *J. Virol.* **68**, 4650 (1994).
41. G. Pantaleo *et al.*, *Nature* **370**, 463 (1994).
42. Z. W. Chen *et al.*, *J. Exp. Med.* **182**, 21 (1995).
43. E. S. Rosenberg *et al.*, *Science* **278**, 1447 (1997).
44. P. M. Garcia *et al.*, *N. Engl. J. Med.* **341**, 394 (1999).
45. T. C. Quinn *et al.*, *N. Engl. J. Med.* **342**, 921 (2000).
46. We acknowledge support from NIH grants CA-50139 (N.L.L), AI-85343 (N.L.L. and D.C.M.), AI-65301 (M.G.L.), AI/GF-41521 (T.B.S.), and AI-42298 (T.B.S.). We are grateful to N. Miller, F. Vogel, M. Forman, K. Reimann, W. Lin, A. Miura, R. Kuhnkuhn, C. Lord, J. Frost, T. Steenbeke, C. Crabbs, J. Yalley-Ogunro, N. Persaud, L. Zhu, and J. Joyce for generous advice, assistance, and reagents.

4 August 2000; accepted 15 September 2000

REPORTS

Imaging Precessional Motion of the Magnetization Vector

Y. Acremann,[1] C. H. Back,[1]* M. Buess,[1] O. Portmann,[1] A. Vaterlaus,[1] D. Pescia,[1] H. Melchior[2]

We report on imaging of three-dimensional precessional orbits of the magnetization vector in a magnetic field by means of a time-resolved vectorial Kerr experiment that measures all three components of the magnetization vector with picosecond resolution. Images of the precessional mode taken with submicrometer spatial resolution reveal that the dynamical excitation in this time regime roughly mirrors the symmetry of the underlying equilibrium spin configuration and that its propagation has a non-wavelike character. These results should form the basis for realistic models of the magnetization dynamics in a largely unexplored but technologically increasingly relevant time scale.

A magnetic moment placed at an angle with respect to a magnetic field will feel a torque that tries to align it along the direction of the magnetic field. Because the magnetic moment has an angular momentum, the torque will cause the magnetic moment to precess. This is the content of Larmor's theorem (*1*). Textbook examples of this theorem are spin resonance phenomena (*2–4*). Because of its picosecond time scale, precessional motion in ferromagnetic elements attracts technological attention; for instance, precessional magnetization reversal launched by picosecond field pulses has been suggested as a possible way of advancing the speed of magnetic recording devices into new time scales (*5*).

This precessional motion has become the target of experiments designed to detect it directly in the time domain (*6–11*) and, to date, one component of the precessing magnetization vector has been measured accurately with subnanosecond resolution. However, precessional motion evolves in the three-dimensional space defined by the three components of the magnetization vector and is a challenge for direct experimental detection. Yet, measuring all three components as they evolve in time provides essential information necessary to develop realistic models of magnetization dynamics on a picosecond time scale. We explored the vectorial precessional mode launched by a picosecond field pulse in a ferromagnet, which, because of its elementary character, allowed us to directly compare the analytical solution of the Larmor equation with the experimental observations. The result is a picture of this mode containing unprecedented details that should form the basis for future modeling of this phenomenon.

The sample used here is a flat, polycrystalline Co disk grown by electron-beam evaporation inside a 400-nm-thick, single-turn aluminum coil (see the optical micrograph in Fig. 1A). The Co disk has a diameter of ≈6 μm and a thickness of ≈20 nm, and is capped with ≈2 nm of Pt for corrosion protection, as the time-resolved experiments are performed at ambient pressure. The magnetic contrast within the Co disk (Fig. 1B) was revealed by spin-polarized scanning electron microscopy (SEMPA) (*12*). The corresponding domain pattern (summarized schematically in Fig. 1C) shows four in-plane magnetized domains arranged to form a closed magnetic flux configuration within the Co disk, thus minimizing the magnetostatic energy (*13*). This closed-flux configuration suggests that the shape anisotropy is the essential mechanism establishing the equilibrium spin configuration of Fig. 1B. In our analysis, we neglect other types of magnetic anisotropies, such as the magneto-crystalline one. The simplest mathematical model capturing the symmetry of the closed-flux configuration associates every point in the disk with cylindrical coordinates (ρ, φ, z), and assigns cylindrical unit vectors $(\vec{e}_\rho, \vec{e}_\varphi, \vec{e}_z)$ to the magnetization vector $(M_\rho, M_\varphi, M_z) = (0, M_0, 0)$ (Fig. 1D).

Applying a sudden small magnetic field along *z* provides the initial torque which will produce a small but finite M_ρ. This initial deviation leads to the motion of $\vec{M}$, described by the Larmor coupled differential equations (*1*) [neglecting the product of small terms (*3*)]

[1]Laboratorium für Festkörperphysik, Eidgenössische Technische Hochschule (ETH) Zürich, CH-8093 Zürich, Switzerland. [2]Institut für Quantenelektronik, ETH Zürich, CH-8093 Zürich, Switzerland.

*To whom correspondence should be addressed. E-mail: back@solid.phys.ethz.ch

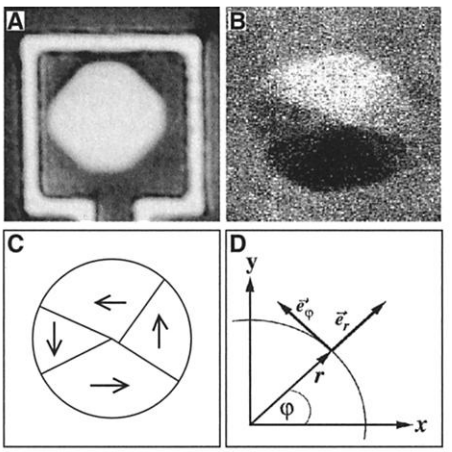

Fig. 1. (**A**) Optical micrograph of the Co dot inside a single-turn coil of Al, evaporated (pressure during growth: 1×10^6 mbar) on quartz glass using standard lift-off technique. The Co dot is sandwiched between two 2-nm-thick Pt buffer layers. (**B**) In SEMPA, the spin polarization of the emitted secondary electrons, excited by a focused electron beam, is measured and is proportional to the magnetization within the beam focus. In the image, the white (black) regions correspond to domains positively (negatively) magnetized along the direction parallel to the horizontal axis. Within the gray regions on the sides, the magnetization is along the vertical direction, as shown by measuring the corresponding polarization component. The closed-flux spin configuration is represented schematically in (**C**). The SEMPA image was taken after the spin dynamics experiments. To prepare a clean surface suitable for SEMPA, the Pt capping layer was removed by soft sputtering and the dot capped with ≈2 nm of Co under ultrahigh vacuum conditions. (**D**) The coordinate system used to model the closed-flux spin configuration is represented.

$$\frac{dM_\varphi}{dt} = 0$$

$$\frac{dM_\rho}{dt} = +|\gamma| N_z \cdot M_z \cdot M_\varphi$$

$$\frac{dM_z}{dt} = -|\gamma| N_\rho \cdot M_\rho \cdot M_\varphi$$

to be solved with the initial conditions $[M_\varphi(t = 0) = M_0]$, $[M_\rho(t = 0) = \Delta \ll M_0]$, and $[M_z(t = 0) = 0]$. The value $|\gamma|$ is the gyromagnetic ratio. N_ρ and N_z are demagnetizing factors determining the ρ and z component of the magnetic field acting on the magnetization vector (because of the closed-flux configuration of Fig. 1B, $N_\varphi = 0$). For a disk with the geometrical dimensions of the one in Fig. 1A, $N_\rho \approx 0.17$ and $N_z \approx (4\pi - 0.17)$ (*14*). This problem contains no free parameters and can be solved analytically: $[M_\varphi = M_0]$, $[M_\rho \propto \cos(2\pi \frac{t}{T})]$, and $[M_z \propto \sin(2\pi \frac{t}{T})]$. The theoretical period T_{th} of the oscillation, calculated by solving the determinantal equation, is $T_{th} = 2\pi(\gamma M_0 \sqrt{N_\rho \cdot N_z})^{-1} = 169$ ps. $M_\rho(t)$ and $M_z(t)$ are phase shifted by $\pi/2$, with the component orthogonal to the applied field pulse (M_ρ) starting first, followed by the component parallel to the field pulse (M_z). This time sequence, including the phase shift, is the essential content of Larmor's theorem and causes the locus of the magnetization vector to be along an orbit in the plane perpendicular to M_φ.

These analytical results are reproduced by the vectorial time-resolved experiment. Figure 2A shows M_z, measured at a location within the disk with equilibrium spin configuration along x, as a function of the time elapsed after the field pulse [details of the vectorial Kerr experiment are described in (*15*)]. A short field pulse originating from the coil (solid line in Fig. 2A) (*16*) launches an oscillatory M_z component, with an experimental period of $T_{exp} \approx 165 \pm 5$ ps. Two experimental features not accounted for by the analytical solution are (i) the decay of the oscillation amplitude (given by the envelope of the graph), which occurs with a time constant of ≈330 ps, and (ii) the shift toward positive values of the oscillatory component. Feature (i) is due to relaxation processes of the magnetization, which, in a more complete theory, are taken into account by the Landau-Lifschitz equation (*5, 7, 9*). Feature (ii) is due to the slow decay of the magnetic field pulse (*16*). $M_y(t)$, measured at the same location as in Fig. 2A, starts to deviate from the equilibrium value before M_z does (Fig. 2B). Comparing the two figures, a phase shift of approximately $\pi/2$ is observed. As a consequence of this shift, the experimental $M_y(t)$ and $M_z(t)$, combined in Fig. 2C in a two-dimensional plot showing M_z versus M_y, describe an orbit that reveals the precessional motion of the magnetization vector predicted by Larmor's theorem. Because of the decay of the oscillatory component, the precessional orbit spirals back to the origin (*17*).

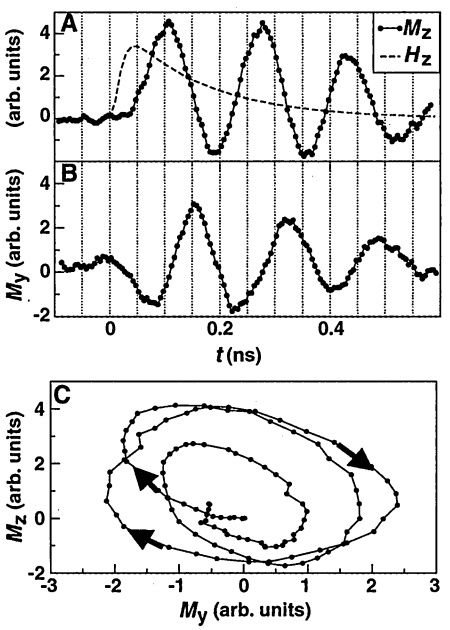

Fig. 2. Results of the time-resolved vectorial Kerr experiment. (**A**) M_z (in aribitrary units) versus time. The curve is measured at a location where the initial spin configuration is along x. (**B**) M_y as a function of time (M_x being constant in time within experimental noise). In agreement with Larmor's theorem, M_y deviates from the equilibrium value before M_z does, and remains ahead of M_z by approximately $\pi/2$. (**C**) The Larmor orbit in the plane perpendicular to x, obtained by combining the results of (A) and (B) into a M_z-versus-M_y plot.

Our vectorial time-resolved experiment with submicrometer spatial resolution was used to produce images of the local precessional mode within the magnetic Co disk. A set of images (Fig. 3), taken at a given delay time, show the spatially resolved x, y, and z components of the local magnetization vector. The in-plane images roughly reproduce the symmetry of the equilibrium spin configuration: the side domains, with equilibrium magnetization along $\pm y$, are visible in the x component of the dynamical magnetization (Fig. 3A), whereas the top (bottom) domains, with equilibrium magnetization along $\pm x$, are visible in the y component of the dynamical magnetization (Fig. 3B and, schematically, Fig. 3D). The z component, which is zero in the equilibrium configuration, reproduces the almost circular symmetry provided by the closed-flux equilibrium state (Fig. 3C). However, despite being symmetric with respect to rotations around the z axis, the dynamical z component reveals a spatial nonuniformity

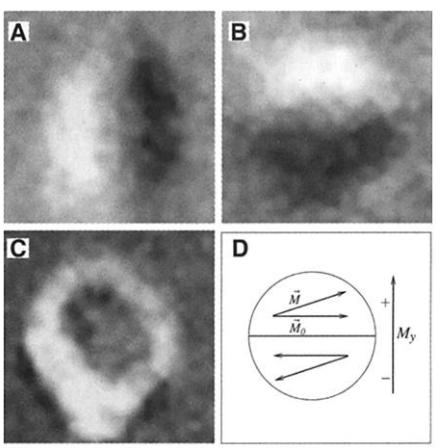

Fig. 3. (**A** and **B**) Spatially resolved images of the magnetization vector at a fixed delay time (180 ps in this figure). To take the images, we scanned the sample under the focusing objective using a piezoelectric stage. (**D**) shows schematically that a field pulse along z (not shown in the figure) activates the $+y$ ($-y$) component of the magnetization within domains with equilibrium spin configuration along $+x$ ($-x$) and leads to the white-black magnetic contrast observed in the in-plane components (**C**).

absent in the equilibrium spin configuration. For instance, the center and the boundary of the dot are in a different precessional state. A closer inspection of images of the in-plane components also reveals a similar spatial nonuniformity, although it is not as explicit because of the smaller signal-to-noise ratio of the in-plane measurements. Although spatial nonuniformities have already been observed (*7*), their origin remained puzzling.

In a sequence of images of $M_z(\vec{r})$ taken at successive times, we are able to follow the buildup and evolution of this nonuniform precessional mode as it occurs in time [Fig. 4 and supplemental Web movie (*18*)]. Precession starts at the boundary with a positive sign (Fig. 4A) (*18*) and appears to propagate into the center (Fig. 4B), where it becomes active at a later time. In Fig. 4C, the precessional mode has reversed its sign and has already started to proceed back to the boundary, where the dynamic component reverses again to positive values (Fig. 4D) and the whole sequence repeats. At first glance, one is tempted to interpret the nonuniform excitation as a wave propagating from the border toward the center and then bouncing back. There are two important factors that exclude the buildup of a precessional wave: (i) an estimate of the time it takes to reach the center leads to a velocity of ≈50 km/s. We estimate that the spin wave group velocity for a $\vec{k}$-vector compatible to the lateral size of the Co disk is at least one order of magnitude smaller than this value (*4*). (ii) Because the magnetization at the boundary is actively precessing, we must assume Neumann conditions at the boundary, i.e., the same boundary conditions used in theoretical studies of the spin wave dynamics in restricted geometries (*4*). This means that the magnetic "membrane" is free to move at the boundary and that waves are reflected without reversing their sign (*19, 20*). Thus, our observation of an apparent sign reversal at the boundary contradicts the hypothesis of a precessional wave. In order to find the origin of this nonuniformity, we plotted (Fig. 4E) $M_z(t)$ obtained from images at the boundary (circles) and at the center (diamonds). Both oscillate, within experimental uncertainty, with the same period. Thus, the magnetic fields acting on the precessional magnetization vector are roughly the same at the boundary and at the center (*21*) and the linearization of the coupled equations is applicable to the central part of the disk as well (*22*). On the other hand, the two curves show two clear differences: (i) the maximum oscillation amplitude at the center is smaller by ≈20% with respect to the boundary, and (ii) the two curves are shifted by an almost constant offset amounting to 10 ± 3 ps. Our calculations of the spatial dependence of the magnetic field produced by the coil reveals a nonuniformity that can be as large as 20% across the disk (the field is strongest at the boundary). This can explain (i) (*23*), but not the offset. The observed time offset suggests that the origin of the nonuniform precessional mode is some delay in the start of the precession. A possible cause for (ii) is Faraday's induction law: The applied magnetic field is only immediately present on the "skin" of the magnetic sample, where the precession starts. The corresponding precessional phase is observed at the center after a delay of the order of $T_{exp} \times d/2\delta \approx$ 10 ps [d being the thickness of the film and δ the skin depth at frequencies corresponding to a 10-ps rise time (*24, 25*)].

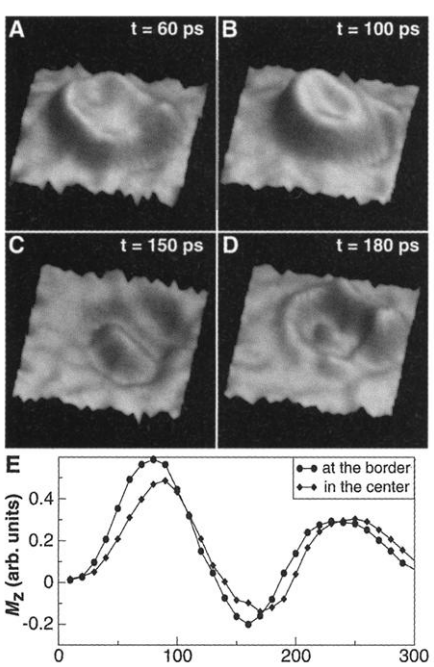

Fig. 4. Spatially resolved images of M_z at different delay times. Going from (**A**) through (**D**), the precessional mode apparently moves toward the center (**B**), reverses to negative values, returns to the boundary (**C**), and bounces back with positive sign from the boundary. In (**E**), $M_z(t)$ evaluated from the images at the boundary (circular points) and at the center of the dot (diamond points) is shown.

Despite strong correlation of the spins, the precession of spin blocks with submicrometer linear size depends only on the local field occurring within each block. This finding supports the theoretical model that was used to explain the final domain pattern obtained after picosecond pulse–induced precessional switching (*5*). The absence of precessional waves at submicrometer scales considerably simplifies the dynamical behavior, which roughly reflects the symmetry of the underlying equilibrium configuration. Small corrections due to eddy currents introduce spatial nonuniformities that are not present in the equilibrium spin configuration and must be taken into account for a realistic model of magnetization dynamics with ultrashort magnetic pulses.

References and Notes

1. L. D. Landau, E. M. Lifshitz, *Mechanics and Electrodynamics* (Pergamon, Oxford, 1972), pp. 211–212.
2. F. Bloch, *Phys. Rev.* **70**, 460 (1946).
3. C. Kittel, *Phys. Rev.* **73**, 155 (1948).
4. J. Jorzick *et al.*, *Phys. Rev. B* **60**, 15194 (1999).
5. C. H. Back *et al.*, *Science* **285**, 864 (1999).
6. W. Dietrich, W. E. Pröbster, P. Wolf, *IBM J. Res. Dev.* **4**, 189 (1960).
7. W. K. Hiebert, A. Stankiewicz, M. R. Freeman, *Phys. Rev. Lett.* **79**, 1134 (1997).
8. J. M. Kikkawa, I. P. Smorchokova, N. Samarth, D. D. Awschalom, *Science* **277**, 1284 (1997).
9. T. M. Crawford, T. J. Silva, C. W. Teplin, C. T. Rogers, *Appl. Phys. Lett.* **74**, 3386 (1999).
10. R. J. Hicken, J. Wu, *J. Appl. Phys.* **85**, 4580 (1999).
11. D. Craik, *Magnetism: Principles and Applications* (Wiley, Chichester, UK, 1995), p. 289.
12. C. Stamm *et al.*, *Science* **282**, 449 (1998).
13. C. Kittel, *Phys. Rev.* **70**, 965 (1946).
14. D.-X. Chen, J. A. Brug, R. B. Goldfarb, *IEEE Trans. Magn.* **27**, 3601 (1991).
15. A femtosecond laser system (100-fs pulse length, 76-MHz repetition rate, wavelength of 800 nm) is used to measure $\vec{M}$ in a pump-probe experiment. A variable optical delay establishes a time delay t between a field-creating pulse and the laser pulse used to probe $\vec{M}$. The frequency-doubled laser pulse is fed into a standard Zeiss polarization-conserving microscope with a high numerical aperture objective (N.A. = 0.95). We detect changes of the perpendicular component of $\vec{M}$ by analyzing the polarization of the reflected light in the polar Kerr effect geometry, with a spatial resolution better than 400 nm. The in-plane components are measured by moving the incident laser beam out of the axis of the objective (spatial resolution ≈ 800 nm) and using the pure transverse Kerr effect. Because the intensity of the reflected beam is detected without polarization analysis, the in-plane components can be separated from the perpendicular one.
16. The magnetic field pulse along z is provided by directing one of the laser pulses onto a biased GaAs photoconductive switch (*26*). When triggered, the switch launches a current pulse into the aluminum single-turn coil shown in Fig. 1A. In a similar coil design, Elezzabi *et al.* (*27*) measured a pulse shape similar to the one in Fig. 2A. The rise time in (*27*) was 12.5 ps. We cannot accurately determine the rise time; however, it is much shorter than the precessional frequency of the magnetic system, so that the precessional motion of $\vec{M}$ can be excited. The shift toward positive values of the oscillatory component is due to the slowly decaying field pulse caused by the recombination processes in the photoconductive switch. Within a numerical simulation of the data in Fig. 2A based on the Landau-Lifshitz equation (*5*), this shift was used to estimate the decay time $\tau_f \approx$ 150 ps (the solid line in Fig. 2A shows the pulse shape estimated with τ_r = 12.5 ps and τ_f = 150 ps). The voltage across the switch is 10 V leading to a maximum current of 200 mA into the 50-ohm device when fully closed. Thus, the maximum field amplitude can be estimated to be less than 500 Oe everywhere on the disk. Because this value is much smaller than the demagnetizing fields ($4\pi M_0$ = 17 kOe for Co), the applied field produces a deviation from the equilibrium spin configuration smaller than 5%, justifying the neglect of quadratic terms in the Larmor equation.
17. The analytical solution of the Larmor equation also predicts the exact shape of the orbits (*3*). The determination of the shape would require measuring M_z and M_y in absolute values.

18. Supplemental Web movie is available at www.sciencemag.org/feature/data/1053788.shl
19. P. M. Fishbane, S. Gasiorowicz, S. T. Thornton, *Physics for Scientists and Engineers* (Prentice-Hall, Upper Saddle River, NJ, ed. 2, 1996), p. 419.
20. H. J. Leisi, *Klassische Physik* (Birkhäuser Verlag, Basel, Switzerland, 1996), pp. 274–276.
21. Nonuniform fields produce different precessional periods. See J. E. Mercereau and R. P. Feynman [*Phys. Rev.* **104**, 63 (1956)].
22. By "center," we mean a region with linear size comparable to the spatial resolution of our experiment.
23. This nonuniformity cannot affect the precessional period because the initial field pulse is one of the "small" quantities that can be neglected in solving the Larmor equation.
24. We use $\delta \approx 200$ nm, from J. D. Jackson [*Classical Electrodynamics* (Wiley, New York, 1962), p. 225, equation 7.85]. On this time scale, the magnetic permeability is taken to be 1 because the magnetization is not yet aligned along the magnetic field direction (H. C. Siegmann and W. Hunziker, personal communication).
25. After this initial delay, eddy currents are negligible for two reasons: the oscillation of the magnetization occurs on a larger time scale and eddy currents do not affect the precessional motion in the present geometry (*3*).
26. M. R. Freeman, J. F. Smyth, *J. Appl. Phys.* **79**, 5898 (1996).
27. A. Y. Elezzabi, M. R. Freeman, *Appl. Phys. Lett.* **68**, 3546 (1996).
28. We gratefully acknowledge financial support by the Swiss National Fund and the Swiss Federal Institute of Technology.

7 July 2000; accepted 8 September 2000

Modulation Instability and Pattern Formation in Spatially Incoherent Light Beams

Detlef Kip,[1,2] Marin Soljacic,[1,3] Mordechai Segev,[1,4]* Eugenia Eugenieva,[5] Demetrios N. Christodoulides[5]

We report on the experimental observation of modulation instability of partially spatially incoherent light beams in noninstantaneous nonlinear media and show that in such systems patterns can form spontaneously from noise. Incoherent modulation instability occurs above a specific threshold that depends on the coherence properties (correlation distance) of the wave packet and leads to a periodic train of one-dimensional filaments. At a higher value of nonlinearity, the incoherent one-dimensional filaments display a two-dimensional instability and break up into self-ordered arrays of light spots. This discovery of incoherent pattern formation reflects on many other nonlinear systems beyond optics. It implies that patterns can form spontaneously (from noise) in diverse nonlinear many-body systems involving weakly correlated particles, such as atomic gases at (or near) Bose-Einstein condensation temperatures and electrons in semiconductors at the vicinity of the quantum Hall regime.

Modulation Instability (MI) is a process that appears in most nonlinear wave systems. Because of MI, small amplitude and phase perturbations (from noise) grow rapidly under the combined effects of nonlinearity and diffraction (or dispersion, in the temporal domain). As a result, a broad optical beam [or a quasi–continuous wave (quasi-CW) pulse] tends to disintegrate during propagation (*1–4*), leading to filamentation (*5*, *6*) or to break up into pulse trains (*1–4*). MI typically occurs in the same parameter region where another universal phenomenon, soliton occurrence, is observed. Solitons are stationary localized wave packets (wave packets that never broaden) that share many features with real particles. For example, their total energy and momentum is conserved even when they interact with one another (*7*). Solitons can be intuitively understood as a result of the balance between the broadening tendency of diffraction (or dispersion) and nonlinear self-focusing. A soliton forms when the localized wave packet induces a potential (via the nonlinearity) and "captures" itself in it, thus becoming a bound state in its own induced potential. In the spatial domain of optics, a spatial soliton forms when a very narrow optical beam induces (through self-focusing) a waveguide structure and guides itself in its own induced waveguide. The relation between MI and solitons is best manifested in the fact that the filaments (or the pulse trains) that emerge from the MI process are actually trains of almost ideal solitons. Therefore, MI can be considered to be a precursor to soliton formation. To date, MI has been systematically investigated in connection with numerous nonlinear processes. Yet traditionally, it was always believed that MI is inherently a coherent process and can only appear in nonlinear systems with a perfect degree of spatial and temporal coherence. On the other hand, recent theoretical work (*8*) has shown that MI can also exist in relation with partially incoherent wave packets or beams. This in turn leads to several important new features: incoherent MI appears only if the "strength" of the nonlinearity exceeds a well-defined threshold that depends on the degree of spatial correlation (coherence). Moreover, by appropriately suppressing MI, new families of solitons are possible that have no counterpart whatsoever in the coherent regime (*9*). Here, we present the experimental observation of modulation instability and pattern formation in partially spatially incoherent light beams in nonlinear media.

Until a few years ago, solitons were considered to be solely coherent entities. However, experimental observations of solitons made of partially spatially incoherent light (*10*) and of temporally and spatially incoherent ("white") light (*11*) have proven that incoherent solitons do exist, and such observations have opened entirely new directions in the field of solitons. Numerous theoretical and experimental works followed soon thereafter, describing bright (*12–15*) and dark (*16*, *17*) incoherent solitons, their interactions (*18*), and stability properties (*19*). The existence of incoherent solitons proves that self-focusing is possible not only for coherent wave packets but also for wave packets upon which the phase is random. The key to their existence is the noninstantaneous nature of the nonlinearity, which responds only to the beam's time-averaged intensity structure and not to the instantaneous highly speckled and fragmented wavefront. In other words, the response time of the nonlinear medium must be much longer than the average time of phase fluctuations across the beam. Thus, the time-averaged intensity induces, through the nonlinearity, a multimode waveguide structure (a potential well that can bind many states), whose guided modes are populated by the optical field with its instantaneous speckled structure. With this noninstantaneous nature of the nonlinearity in mind, we were motivated to find out whether patterns can form spontaneously on a partially coherent uniform beam through the interplay between nonlinearity and diffraction. As a first step, we have shown theoretically (*8*) that a uniform partially incoherent wave front is unstable in such media, provided that the nonlinearity exceeds a well-defined threshold set by the coherence properties. Above that threshold, MI should occur, and patterns should form.

[1]Physics Department and Solid State Institute, Technion, Haifa 32000, Israel. [2]Physics Department, Universität Osnabrück, 49069 Osnabrück, Germany. [3]Physics Department, Princeton University, Princeton, NJ 08544, USA. [4]Department of Electrical Engineering, Princeton University, Princeton, NJ 08544, USA. [5]Electrical Engineering and Computer Science Department, Lehigh University, Bethlehem, PA 18015, USA.

*To whom correspondence should be addressed. E-mail: msegev@techunix.technion.ac.il